Effects of interatomic potential on fracture behaviour in single- and bicrystalline tungsten: Supplementary material

S1. 2NN-MEAM FORMALISM AND FITTING PROCEDURE

A. 2NN-MEAM formalism

Within the 2NN-MEAM framework [1, 2], the total potential energy for a set of particles is given as

$$E = \sum_i F_i(\bar{\rho}_i) + \sum_i \sum_{j \neq i} S_{ij}\phi_{ij}(r_{ij}) \tag{S1}$$

where $F_i(\bar{\rho}_i) = AE_c(\bar{\rho}_i/\bar{\rho}_0)\ln(\bar{\rho}_i/\bar{\rho}_0)$ represents the embedding energy associated with particle i subjected to the background electron density $\bar{\rho}_i$. Moreover, $\bar{\rho}_0$ is the background electron density of the reference structure, while A is an adjustable parameter [2] and E_c is the cohesive energy. The function ϕ_{ij} is the pair interaction contribution between ions i and j, separated by the distance r_{ij}, while S_{ij} is a screening function (see below). Following Baskes [3], we chose the background electron density as a weighted superpositioning of a spherical $\rho_i^{(0)}$ and three angular dependent partial contributions, $\rho_i^{(1)}$-$\rho_i^{(3)}$, to the total electron density. They are constructed through spatial invariants and given as

$$\rho_i^{(0)} = \sum_{j \neq i} f_j^{(0)}(r_{ij}) \tag{S2}$$

$$\rho_i^{(1)} = \left[\sum_{\alpha} \left[\sum_{j \neq i} f_j^{(1)}(r_{ij}) \frac{r_{ij}^{\alpha}}{r_{ij}} \right]^2 \right]^{1/2} \tag{S3}$$

$$\rho_i^{(2)} = \left[\sum_{\alpha,\beta} \left[\sum_{j \neq i} f_j^{(2)}(r_{ij}) \frac{r_{ij}^{\alpha} r_{ij}^{\beta}}{r_{ij}^2} \right]^2 - \frac{1}{3} \left[\sum_{j \neq i} f_j^{(2)}(r_{ij}) \right]^2 \right]^{1/2} \tag{S4}$$

$$\rho_i^{(3)} = \left[\sum_{\alpha,\beta,\gamma} \left[\sum_{j \neq i} f_j^{(3)}(r_{ij}) \frac{r_{ij}^{\alpha} r_{ij}^{\beta} r_{ij}^{\gamma}}{r_{ij}^3} \right]^2 \right]^{1/2} \tag{S5}$$

where r_{ij}^{α} represents the individual components of the interatomic distance vector ($\alpha = x, y, z$). We emphasize that for the herein fitted 2NN-MEAM potential, Eq. (S5) does not have the orthogonal format introduced in [4]. The functions $f_j^{(h)}$ ($h = 0 - 3$) in Eqs. (S2) to (S5) are the pairwise electronic density functions given by

$$f_j^{(h)}(r_{ij}) = \exp[-\beta^{(h)}(r_{ij}/r_e - 1)] \tag{S6}$$

for which $\beta^{(h)}$ are fitting parameters and r_e is the nearest neighbour distance in the reference structure. The electron background density is given by

$$\bar{\rho}_i = \frac{2\rho_i^{(0)}}{1 + \exp[-\Gamma_i]} \tag{S7}$$

where

$$\Gamma_i = \sum_{h=1}^{3} t^{(h)} [\rho_i^{(h)}/\rho_i^{(0)}]^2 \tag{S8}$$

which contains three weight parameters, $t^{(h)}$ that dictate the individual contributions to the total background density.

The pairwise screening function S_{ij} in Eq. (S1) is given by the product of the screening factors from all neighbouring particles, i.e.,

$$S_{ij} = \prod_{k \neq i,j} S_{ikj} \tag{S9}$$

for which S_{ikj} is the screening between particles i and j due to k, is computed based on an elliptic geometry construction as outlined in [1, 2, 5]. Thus, the screening is governed by the geometry of an outer and inner ellipse, whose semi-minor axes are characterized by C_{min} and C_{max}. Then the screening function for the i, j, k-triplet is given by

$$S_{ikj} = f_c\left[\frac{C - C_{min}}{C_{max} - C_{min}}\right] \tag{S10}$$

where f_c is the smooth function

$$f_c(x) = \begin{cases} 1 & x \geq 1 \\ (1-(1-x^4))^2 & 0 \leq x < 1, \\ 0 & x \leq 0. \end{cases} \tag{S11}$$

This yields two additional fitting parameters, C_{min} and C_{max}.

The pair potential, $\phi_{ij}(r_{ij})$, is determined by fitting the total energy to a variant of Rose's universal binding energy relation (UBER) [6, 7],

$$E(a^*) = -E_c\left(1 + a^* + \frac{\alpha d a^{*3}}{a^* + \alpha}\right)\exp[-a^*] \tag{S12}$$

where is defined as $a^* = \alpha(r_{ij}/r_e - 1)$. The parameter α is given by $\alpha = \sqrt{9B\Omega/E_c}$ where B is the bulk modulus and Ω is the equilibrium atomic volume of the reference structure.

B. Fitting procedure

The fitting of the 2NN-MEAM potential was performed using the open-source MEAM parameter calibration (MPC) tool [8]. This software allows for optimization of the MEAM parameters to reproduce DFT data that serves as input (see section S2, for details about the DFT modelling). For the fitting procedure we established two DFT-based databases: one that comprises data to which the potential was fitted and one that contains data that was used to evaluate the resulting potential. For fitting such potentials it is standard procedure to include the cohesive energy (8.66 eV [9]), the lattice parameter (3.165 Å [10]) and the elastic constants at 0 K ($C_{11} = 533$ GPa, $C_{12} = 205$ GPa and $C_{44} = 163$ GPa [9]), which we adopted for the present potential. Moreover, when considering low coordination input for the fitting, it is customary to include the monovacancy formation energy. However, since fitting the potential to reproduce the vacancy formation energy typically leads to low surface energies, which is a common deficiency among EAM type potentials, we opted to use surface energies as input for the fitting to ensure improved representation of the fracture toughness. Specifically, the potential was fitted to the unrelaxed surface energies of the {100}, {110} and {111} surfaces, which were found to correspond to 3.93, 3.20 and 3.46 J/m^2, respectively. Moreover, to reproduce the plastic deformation mechanisms accurately, we fitted the potential to reproduce the generalized stacking fault energy for the (110)[1$\bar{1}$1] slip system. Beside these properties we used the structural energy differences of between BCC and the hypothetical FCC and HCP phases, $\Delta E_{BCC\to FCC}$ and $\Delta E_{FCC\to HCP}$, as derived in [2] by means of the CALPHAD method, and the energy-volume curves for the BCC and hypothetical FCC and HCP (with $c/a = \sqrt{8/3}$) phases from DFT. No effort was made to fit the potential to reproduce self-interstitial configurations. Thus, the resulting potential inaccurately predicts the [110] self-interstitial to be the ground state. To avoid unrealistic blunting of the crack tip, in line with the work of Ko and Lee [11], we adopted a relatively long cutoff distance r_c (5.4 Å) and cutoff region Δr (2.5 Å).

Several potentials were generated and tested. Although there were other fits that reproduced the fitting data better than that given here, the one chosen here was found to have better transferability in terms of general fracture behaviour and plastic mechanisms. It also did not suffer from artificial crack branching, which some of the better fits did. Hence it was chosen for this investigation and its parameters (except default LAMMPS 2NN-MEAM parameters) can be seen in TABLE S1. Most of the fracture related evaluation properties are described in sections III.A and III.B of the main article.

Table S1. 2NN MEAM parameters of MEAM-2 for BCC tungsten. Here, E_{coh}, r_e and B are in eV, Å and GPa units, respectively. These parameters are defined in [2].

Parameter	Values	Parameters	Values	Parameters	Values
E_c	8.660	$\beta^{(1)}$	2.500	$t^{(2)}$	0.3331
r_e	2.740	$\beta^{(2)}$	0.3695	$t^{(3)}$	-5.6479
B	309.15	$\beta^{(3)}$	0.311	C_{min}	0.5177
A	0.400	$t^{(0)}$	1.00	C_{max}	2.7788
$\beta^{(0)}$	6.1252	$t^{(1)}$	2.376	d	0.0

Using MEAM-2, we have also investigated the core structure of $\frac{a}{2}\langle 111\rangle$ screw dislocation. A 3-fold symmetric core structure is revealed for the screw dislocation by MEAM-2. This is not in agreement with the DFT prediction of compact, non-degenerate screw dislocation core structure [12, 13]. The Peierls stress computed using the procedure described in [12] is 2.76 GPa which is comparable to 2.4 GPa predicted in [14] by DFT.

S2. DENSITY FUNCTIONAL THEORY MODELLING

All DFT simulations in this work were performed using the Vienna *ab initio* simulation package (VASP) [15–18]. For describing the valence-core interaction we used the projector augmented wave (PAW) approach [19] with the valence electron description for W comprising the $5d^4 6s^2$ states. We chose the kinetic energy cutoff for the plane-wave basis set and k-point density such that the ground state energy was well-converged. To achieve this, we used a kinetic energy cutoff of 450 eV and a k-point grid for the first Brillouin zone of the primitive BCC cell corresponding to a Γ-centered $14 \times 14 \times 14$ grid generated by means of the Monkhorst-Pack method [20]. For the calculations, we used smearing based on the Methfessel-Paxton method with a width corresponding to 0.1 eV [21]. The exchange-correlation functional is described by the generalized gradient approximation using the Perdew, Burke and Ernzerhof (PBE) formula [22, 23].

S3. CYLINDER RADIUS CONVERGENCE FOR CRACK SIMULATIONS

The size of the K-dominant region extending radially from the crack tip decides the optimal radius (including the thickness of the fixed atoms region) of the cylindrical setup for atomistic crack simulations. Consequently, this is measured by plotting the K_I^{crit} values of a brittle crack system (for example, Σ5, $(310)[001]$) against increasing radius of the cylinder (see FIG. S1). Here brittle GB crack system is chosen as the procedure is inapplicable for ductile systems. The radius for which the change in K_I^{crit} is of the order of 0.025 MPa $m^{1/2}$ is then considered for the crack simulations. This is found to occur around $r_{cyl} = 120$ Å (see FIG. S1), beyond which the fracture toughness is considered well-converged. In our crack simulations, we have used $r_{cyl} \approx 160$ Å for all the crack systems.

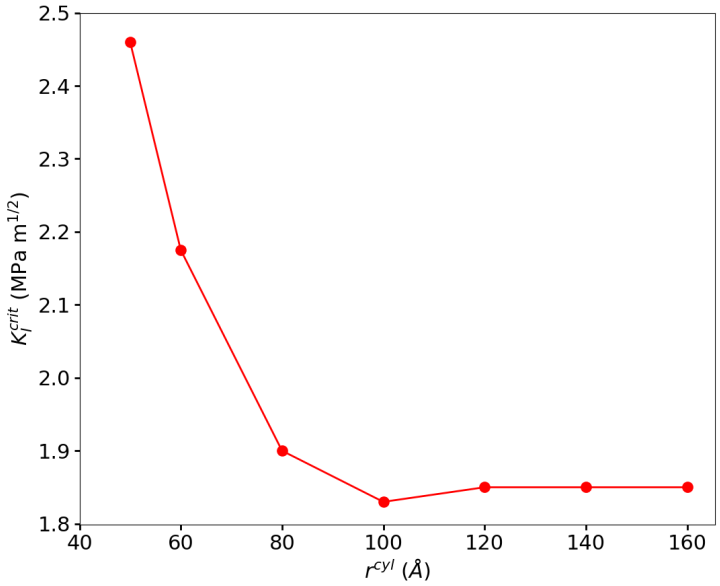

Fig. S1. K_I^{crit} vs cylinder radius (r_{cyl}) of Σ5, $(310)[001]$ crack setup.

S4. BULK, DEFECT, SURFACE AND GRAIN BOUNDARY PROPERTIES

In Table S2 we have compiled the raw data from the evaluation of bulk, defect and surface properties of the semi-empirical potentials. Along with the data we present relevant experimental data and data from DFT modelling for comparison. In addition to these properties, we have compared the relative timings of the potentials to assess the speed. For this purpose, the computational cost (t_{cost}) associated with each potential was evaluated using a benchmark approach similar to that outlined in [24]. Thus we evaluated the timings associated with simulating 3456 BCC tungsten atoms at 300 K for 10^5 timesteps on a

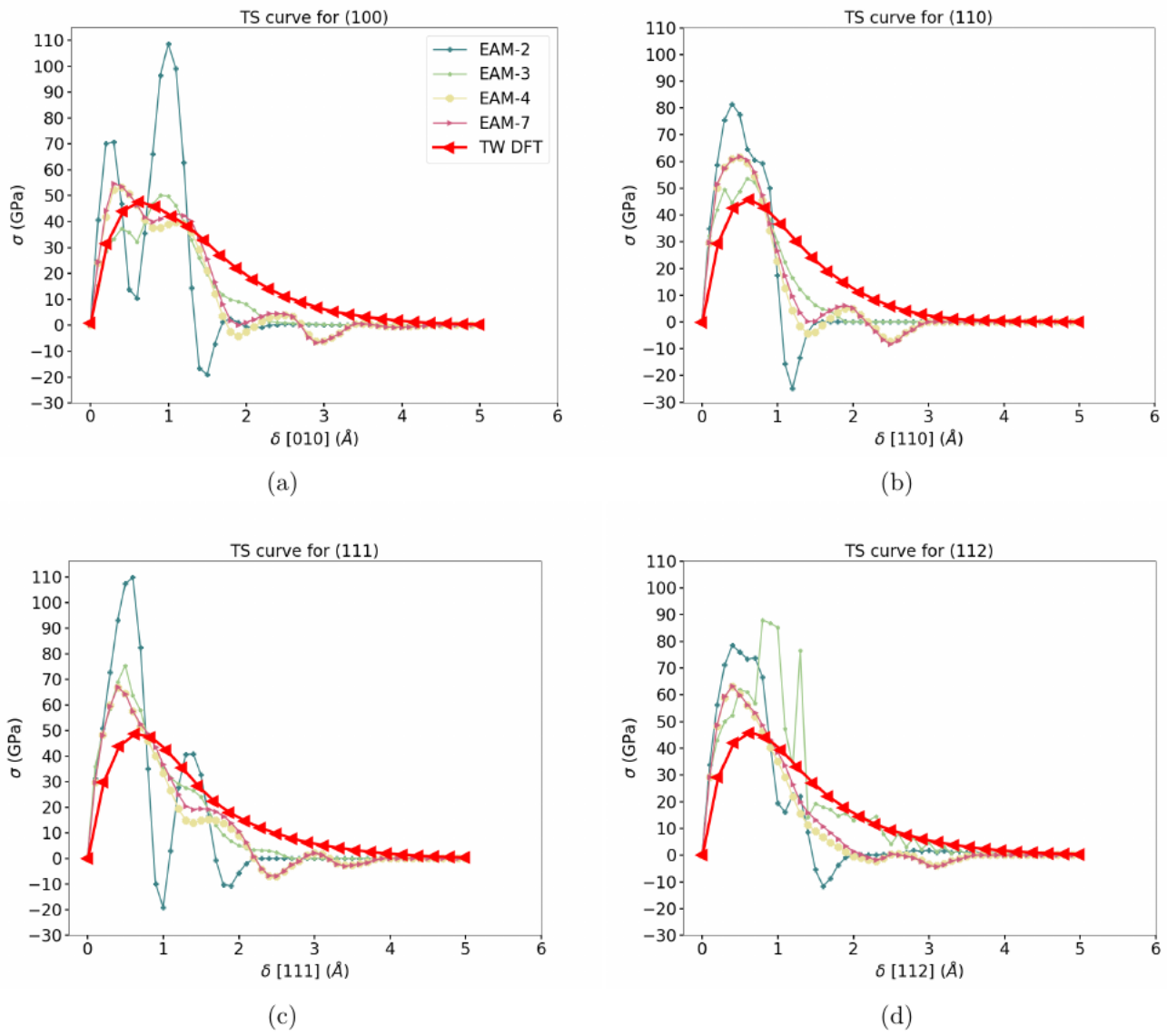

Fig. S2. Comparison of TS curves of (a) (100), (b) (110), (c) (111) and (d) (112) surfaces with DFT data computed in This Work. Here, δ is the separation distance.

single CPU. In Table S3, we have evaluated grain boundary properties for a number of grain boundaries. Our focus is on grain boundary energy, ideal energy release rate.

The traction-separation (TS) curves of single-crystals, for the creation of {100}, {110}, {111} and {112} surfaces using the EAM-2, EAM-3, EAM-4, EAM-7 potentials are presented in FIG. S2. These are the potentials that did not predict a positively skewed bell-shape, but rather displayed a quite oscillating behaviour.

The TS behaviour of the interfaces of $\Sigma 3, (112)[1\bar{1}0]$ and $\Sigma 5, (310)[001]$ GBs using the EAM-2, EAM-3, EAM-4, EAM-7 potentials can be seen in FIG. S3. The TS curves that resemble the DFT characteristics are provided in the main article, see FIG.5 for surface TS curves and FIG.6 for TS curves of GB interfaces. It can be concluded that not all the potentials considered in this work have given single peak, smooth and positive stress valued TS curves.

Table S2. Comparison of bulk and surface properties obtained from MEAM and EAM potentials with DFT data. All parameters are defined in Sects. 3 and 4 of the main article. TW indicates DFT data from This Work. t_{cost} is the normalized computational cost of potentials, relative to EAM-1.

		Potentials										
Properties	Units	EAM-1	EAM-2	EAM-3	EAM-4	EAM-5	EAM-6	EAM-7	MEAM-1	MEAM-2	DFT	Expt
a_0	Å	3.165	3.166	3.164	3.143	3.159	3.166	3.149	3.164	3.160	3.18[TW]	3.165[10]
											3.14[25]	3.164[26]
E_{coh}	eV	-8.90	-8.91	-8.91	-8.90	-8.90	-8.76	-8.90	-8.66	-8.66	-8.48[27]	-8.66[9]
												-8.9[26]
E_{vac}	eV	3.63	3.80	3.58	3.49	3.67	3.58	3.82	3.95	4.13	3.51[TW]	3.6 [28]
											3.56[29]	3.5, 4.1[26]
C_{11}	GPa	522.5	532.6	522.5	523.0	532.5	522.5	523.2	535.5	530.4	544[TW]	533[9]
											517[30]	523[25]
											513[29]	529[31]
C_{12}	GPa	204.5	205.0	204.5	203.0	205.0	204.2	202.3	205.8	193.9	198[TW]	205[9]
											199[29]	209[31]
											200[32]	
C_{44}	GPa	160.7	163.2	160.7	160.0	163.1	160.8	161.0	163.6	178.5	149[TW]	163[9]
											142[29]	160[33]
$\gamma_{us,\{110\}}$	J/m^2	1.12	2.02	1.38	1.73	1.58	1.82	1.72	1.70	1.79	1.80[TW]	
											1.25[29]	
$\gamma_{us,\{112\}}$	J/m^2	1.30	2.33	1.59	1.97	1.81	2.10	1.94	1.95	2.07	1.90[TW]	
γ_{ut}	J/m^2	0.90	1.82	1.07	1.58	1.27	1.49	1.60	1.41	1.48	1.60[TW]	
$\gamma_{(100)}$	J/m^2	2.93	2.98	2.99	2.76	2.91	2.98	2.96	3.87	3.87	3.93[TW]	6.00[34]
											2.45[29]	
											4.87[29]	
											4.64[35]	
$\gamma_{(110)}$	J/m^2	2.60	2.63	2.57	2.48	2.69	2.58	2.65	3.42	3.38	3.20[TW]	4.30[34]
											2.00[29]	3.25[36]
											3.98[29]	
											4.00[35]	
$\gamma_{(111)}$	J/m^2	3.29	3.32	3.25	3.01	3.28	3.31	3.24	4.00	4.05	3.46[TW]	
											2.16[29]	
											4.49[29]	
											4.45[35]	
$\gamma_{(112)}$	J/m^2	3.08	3.11	2.99	2.95	3.07	3.06	3.13	3.97	3.79	3.44[TW]	
											3.37[12]	
											4.18[35]	
$\gamma_{(114)}$	J/m^2	3.12	3.15	3.07	2.94	3.15	3.12	3.14	3.96	3.88		
$\gamma_{(115)}$	J/m^2	3.17	3.21	3.16	3.58	3.11	3.16	3.35	3.97	3.99		
$\gamma_{(223)}$	J/m^2	3.20	3.23	3.14	3.31	3.23	3.20	3.45	3.92	3.97		
$\gamma_{(334)}$	J/m^2	3.24	3.28	3.19	3.54	3.28	3.25	3.63	3.96	4.02		
$\gamma_{(310)}$	J/m^2	3.02	3.06	3.01	3.11	3.02	3.03	3.24	3.89	3.92	4.30[35]	
$\sigma_{coh}^{(100)}$	GPa	59.98	107.94	50.37	53.35	56.44	67.78	54.32	43.71	44.37	47.71[TW]	
$\sigma_{coh}^{(110)}$	GPa	53.58	81.42	53.63	61.23	61.27	64.49	61.93	43.78	42.59	45.77[TW]	
$\sigma_{coh}^{(111)}$	GPa	50.88	109.22	61.30	66.45	60.30	71.69	66.74	54.54	54.33	48.76[TW]	
$\sigma_{coh}^{(112)}$	GPa	49.50	78.40	54.66	62.79	58.23	65.31	63.13	48.07	47.63	45.73[TW]	
$\delta_{max,sep}^{(100)}$	Å	3.3	2.45	2.7	3.8	3.0	2.8	3.8	3.4	3.4	4.8[TW]	
$\delta_{max,sep}^{(110)}$	Å	1.9	1.8	2.0	3.2	1.8	1.7	3.2	3.0	3.0	4.0[TW]	
$\delta_{max,sep}^{(111)}$	Å	2.7	2.25	3.0	4.0	2.9	3.0	4.0	3.9	3.9	5.0[TW]	
$\delta_{max,sep}^{(112)}$	Å	2.4	2.3	4.1	4.0	2.7	2.8	4.0	3.6	3.6	5.0[TW]	
t_{cost}	unitless	1.00	0.42	1.20	1.07	0.57	2.68	1.24	15.71	12.46		

Table S3. Comparison of GB energies, γ_{GB}, ideal energy release rate, G_I^{GB} (Eq. (5) in main article) and cohesive strength, σ_{coh}^{GB}, of GBs obtained from MEAM and EAM potentials with DFT data. Lack of data in the table reflects unavailability of corresponding reference data. The DFT data marked with *, indicates that it is for a GB shifted along interface.

		Potentials									
Property	Units	EAM-1	EAM-2	EAM-3	EAM-4	EAM-5	EAM-6	EAM-7	MEAM-1	MEAM-2	DFT
						$\Sigma3$, 109.5° $(111)_1(\bar{1}\bar{1}1)_2/[\bar{1}10]$					
γ_{GB}	J/m^2	2.37	2.74	2.51	2.60	2.52	2.54	2.89	2.37	2.54	2.40[37]
G_I^{GB}	J/m^2	4.20	3.90	3.99	3.42	4.04	4.07	3.60	5.63	5.56	5.40[37]
σ_{coh}^{GB}	GPa	40.77	57.93	37.15	46.32	45.28	52.33	48.21	38.91	38.73	-
						$\Sigma3$, 70.5° $(112)_1(\bar{1}\bar{1}2)_2/[\bar{1}10]$					
γ_{GB}	J/m^2	0.39	0.76	0.47	0.75	0.53	0.59	0.92	0.62	0.65	0.65[37]
G_I^{GB}	J/m^2	5.77	5.46	5.53	5.16	5.61	5.53	5.34	7.32	6.93	6.93[37]
σ_{coh}^{GB}	GPa	46.65	84.85	50.26	50.68	57.39	67.06	52.39	46.9	47.99	42.23^{TW}
						$\Sigma5$, 36.9° $(310)_1(3\bar{1}0)_2/[001]$					
γ_{GB}	J/m^2	2.04	2.23	2.02	2.01	2.03	2.05	2.38	2.20	2.38	2.25*,[37]
G_I^{GB}	J/m^2	4.01	3.90	4.00	3.91	4.01	4.01	4.11	5.58	5.46	5.93*,[37]
σ_{coh}^{GB}	GPa	38.06	80.76	41.36	42.16	46.82	60.40	41.96	33.93	33.27	34.75^{*,TW}
						$\Sigma9$, 38.9° $(114)_1(\bar{1}\bar{1}4)_2/[\bar{1}10]$					
γ_{GB}	J/m^2	2.03	3.45	2.34	2.81	2.18	2.24	3.11	2.30	2.51	2.50[37]
G_I^{GB}	J/m^2	4.21	2.86	3.81	3.08	4.13	4.01	3.18	5.62	5.25	5.73[37]
σ_{coh}^{GB}	GPa	39.09	52.08	40.92	42.69	41.81	52.20	44.82	38.04	41.07	-
						$\Sigma17b$, 86.6° $(2\bar{2}3)_1(\bar{2}23)_2/[110]$					
γ_{GB}	J/m^2	1.94	2.77	2.12	2.79	2.19	2.21	3.16	2.19	2.38	-
G_I^{GB}	J/m^2	4.46	3.69	4.16	3.82	4.26	4.19	3.24	5.65	5.55	-
σ_{coh}^{GB}	GPa	44.33	58.18	42.35	41.09	48.06	57.18	43.44	30.5	41.56	-
						$\Sigma17b$, 93.4° $(3\bar{3}4)_1(\bar{3}34)_2/[110]$					
γ_{GB}	J/m^2	2.18	3.15	2.33	2.89	2.39	2.38	3.16	2.36	2.59	2.52[37]
G_I^{GB}	J/m^2	4.31	3.41	4.05	4.19	4.17	4.13	4.10	5.56	5.45	5.45[37]
σ_{coh}^{GB}	GPa	39.80	60.12	41.06	43.70	45.59	55.51	45.45	32.70	41.95	-

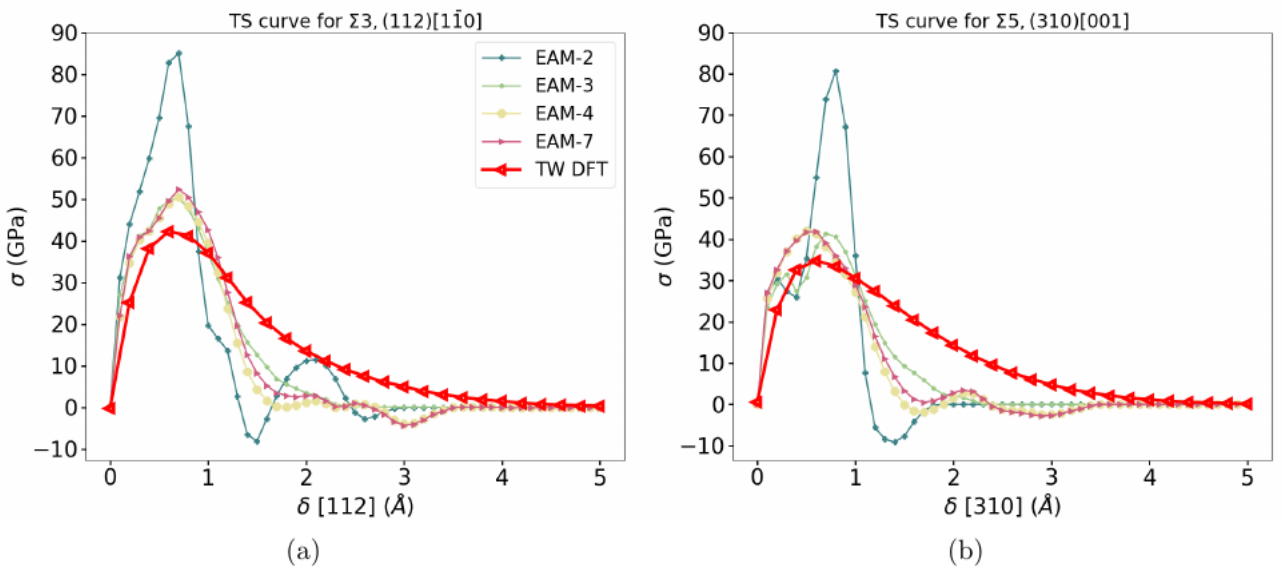

Fig. S3. Comparison of TS curves of (a) Σ3, $(112)[1\bar{1}0]$ and (b) Σ5, $(310)[001]$GB with DFT data computed in This Work. Here, δ is the separation distance.

S5. ANALYTICAL CRITICAL STRESS INTENSITY FACTORS

In Table S4 and S5, we have compiled analytical data for critical stress intensity factors (K_{IG}: Eq. (1), K_{IE}: Eq. (7), K_{IT}: Eq. (9) in the main paper).

Table S4. Analytical critical stress intensity factors (K_{IG}: Eq. (1), K_{IE}: Eq. (7), K_{IT}: Eq. (9), from the main article, in units of MPa $m^{1/2}$) and plastic tendency, T_{pl}, which is dimensionless (Eq. (11)) in single-crystal crack systems.

Crack system	EAM-1				EAM-2				EAM-3			
	K_{IG}	K_{IE}	K_{IT}	T_{pl}	K_{IG}	K_{IE}	K_{IT}	T_{pl}	K_{IG}	K_{IE}	K_{IT}	T_{pl}
(001)[0$\bar{1}$0]	1.61	2.52	2.26	1.40	1.64	3.42	3.24	1.98	1.63	2.79	2.46	1.51
(001)[1$\bar{1}$0]	1.61	2.76	2.48	1.54	1.64	3.74	3.55	2.16	1.63	3.06	2.69	1.65
(110)[$\bar{1}$10]	1.52	2.10	1.88	1.24	1.54	2.83	2.69	1.74	1.51	2.32	2.04	1.35
(01$\bar{1}$)[$\bar{1}$00]	1.52	2.33	2.09	1.37	1.54	3.16	3.00	1.94	1.51	2.58	2.27	1.51
(111)[11$\bar{2}$]	1.71	2.00	1.79	1.05	1.74	2.71	2.57	1.48	1.70	2.21	1.95	1.15
(111)[1$\bar{1}$0]	1.71	2.15	1.93	1.13	1.74	2.91	2.76	1.59	1.70	2.38	2.09	1.23
(112)[$\bar{1}$10]	1.69	1.97	1.77	1.05	1.71	2.67	2.53	1.48	1.67	2.18	1.92	1.15
(114)[1$\bar{1}$0]	1.66	2.10	1.88	1.13	1.69	2.83	2.69	1.59	1.65	2.32	2.04	1.24
($\bar{1}\bar{1}$5)[1$\bar{1}$0]	1.68	2.17	1.94	1.16	1.70	2.93	2.78	1.63	1.68	2.40	2.11	1.26
	EAM-4				EAM-5				EAM-6			
	K_{IG}	K_{IE}	K_{IT}	T_{pl}	K_{IG}	K_{IE}	K_{IT}	T_{pl}	K_{IG}	K_{IE}	K_{IT}	T_{pl}
(001)[0$\bar{1}$0]	1.57	3.13	2.99	1.91	1.62	3.02	2.71	1.67	1.63	3.21	2.90	1.79
(001)[1$\bar{1}$0]	1.57	3.40	3.25	2.08	1.62	3.30	2.95	1.82	1.63	3.51	3.18	1.95
(110)[$\bar{1}$10]	1.49	2.58	2.47	1.66	1.56	2.50	2.24	1.44	1.54	2.66	2.41	1.59
(01$\bar{1}$)[$\bar{1}$00]	1.49	2.89	2.76	1.86	1.56	2.79	2.50	1.61	1.54	2.97	2.68	1.77
(111)[11$\bar{2}$]	1.64	2.48	2.37	1.45	1.72	2.39	2.15	1.25	1.71	2.54	2.30	1.34
(111)[1$\bar{1}$0]	1.64	2.65	2.53	1.55	1.72	2.56	2.30	1.33	1.71	2.73	2.47	1.44
(112)[$\bar{1}$10]	1.70	2.43	2.32	1.08	1.74	2.35	2.11	1.22	1.68	2.51	2.27	1.35
(114)[1$\bar{1}$0]	1.62	2.58	2.47	1.53	1.69	2.50	2.24	1.33	1.67	2.66	2.41	1.45
($\bar{1}\bar{1}$5)[1$\bar{1}$0]	1.78	2.67	2.55	1.43	1.68	2.58	2.31	1.38	1.68	2.75	2.50	1.49
	EAM-7				MEAM-1				MEAM-2			
	K_{IG}	K_{IE}	K_{IT}	T_{pl}	K_{IG}	K_{IE}	K_{IT}	T_{pl}	K_{IG}	K_{IE}	K_{IT}	T_{pl}
(001)[0$\bar{1}$0]	1.62	3.13	3.02	1.86	1.88	3.14	2.86	1.52	1.90	3.28	2.98	1.57
(001)[1$\bar{1}$0]	1.62	3.38	3.26	2.01	1.88	3.42	3.12	1.66	1.90	3.58	3.26	1.71
(110)[$\bar{1}$10]	1.54	2.56	2.47	1.61	1.48	2.60	2.36	1.59	1.78	2.72	2.47	1.39
(01$\bar{1}$)[$\bar{1}$00]	1.54	2.89	2.79	1.81	1.48	2.90	2.64	1.78	1.78	3.03	2.75	1.55
(111)[11$\bar{2}$]	1.70	2.48	2.39	1.41	1.91	2.50	2.26	1.19	1.95	2.59	2.36	1.21
(111)[1$\bar{1}$0]	1.70	2.63	2.54	1.49	1.91	2.66	2.42	1.27	1.95	2.79	2.53	1.30
(112)[$\bar{1}$10]	1.85	2.42	2.33	1.26	1.90	2.45	2.23	1.17	1.96	2.56	2.33	1.19
(114)[1$\bar{1}$0]	1.67	2.56	2.47	1.48	1.64	2.60	2.36	1.44	1.91	2.72	2.47	1.30
($\bar{1}\bar{1}$5)[1$\bar{1}$0]	1.73	2.65	2.56	1.48	1.75	2.68	2.44	1.39	1.93	2.81	2.55	1.32

Table S5. Analytical critical stress intensity factors (K_{IG}: Eq. (1), K_{IE}: Eq. (7), K_{IT}: Eq. (9), in units of MPa $m^{1/2}$) for bicrystal crack systems and plastic tendency, T_{pl}, which is dimensionless (Eq. (11)). Lack of data in the table means either the value could not be calculated due to the ductile behaviour or the corresponding value is not available in the literature [38, 39]. Details of the GBs are given in Table 2 of the main article. "pr.dir" refers to crack propagation direction.

GB, crack system	EAM-1				EAM-5				EAM-6			
Σ,(plane)[front][pr.dir]	K_{IG}	K_{IE}	K_{IT}	T_{pl}	K_{IG}	K_{IE}	K_{IT}	T_{pl}	K_{IG}	K_{IE}	K_{IT}	T_{pl}
Σ3,(111)[1$\bar{1}$0][$\bar{1}\bar{1}$2]	1.37	2.15	1.93	1.41	1.35	2.56	2.30	1.70	1.35	2.73	2.47	1.83
Σ3,(111)[1$\bar{1}$0][11$\bar{2}$]	1.37	2.15	1.93	1.41	1.35	2.56	2.30	1.70	1.35	2.73	2.47	1.83
Σ3,(112)[1$\bar{1}$0][$\bar{1}\bar{1}$1]	1.60	1.97	1.77	1.11	1.59	2.35	2.11	1.33	1.57	2.51	2.27	1.45
Σ3,(112)[1$\bar{1}$0][11$\bar{1}$]	1.60	3.04	2.72	1.70	1.59	3.65	3.27	2.06	1.57	3.87	3.50	2.23
Σ5,(310)[001][1$\bar{3}$0]	1.34	2.16	1.94	1.45	1.35	2.60	2.33	1.72	1.34	2.76	2.49	1.86
Σ5,(310)[001][$\bar{1}$30]	1.34	2.16	1.94	1.45	1.35	2.60	2.33	1.72	1.34	2.76	2.49	1.86
Σ9,(114)[1$\bar{1}$0][22$\bar{1}$]	1.37	2.86	2.57	1.87	1.37	3.44	3.08	2.25	1.34	3.65	3.30	2.46
Σ17b,(2$\bar{2}$3)[110][3$\bar{3}\bar{4}$]	1.41	1.87	1.68	1.19	1.39	2.24	2.01	1.45	1.36	2.39	2.16	1.59
Σ17b,(3$\bar{3}$4)[110][$\bar{2}$23]	1.38	1.90	1.70	1.23	1.38	2.28	2.04	1.48	1.35	2.42	2.19	1.62

	MEAM-1				MEAM-2				Möller[38, 39]			
Σ,(plane)[front][pr.dir]	K_{IG}	K_{IE}	K_{IT}	T_{pl}	K_{IG}	K_{IE}	K_{IT}	T_{pl}	K_{IG}	K_{IE}	K_{IT}	T_{pl}
Σ3,(111)[1$\bar{1}$0][11$\bar{2}$]	1.60	2.66	2.42	1.55	1.61	2.79	2.53	1.57	1.38	2.06	1.77	-
Σ3,(111)[1$\bar{1}$0][$\bar{1}\bar{1}$2]	1.60	2.66	2.42	1.67	1.61	2.79	2.53	1.57	1.38	2.06	-	-
Σ3,(112)[1$\bar{1}$0][11$\bar{1}$]	1.83	2.45	2.23	1.22	1.80	2.56	2.33	1.29	1.59	1.89	1.62	-
Σ3,(112)[1$\bar{1}$0][$\bar{1}\bar{1}$1]	1.83	3.79	3.45	1.89	1.80	3.97	3.61	2.00	1.59	2.91	-	-
Σ5,(310)[001][1$\bar{3}$0]	1.59	2.70	2.46	1.54	1.60	2.81	2.56	1.60	-	-	-	-
Σ5,(310)[001][$\bar{1}$30]	1.59	2.70	2.46	1.54	1.60	2.81	2.56	1.60	-	-	-	-
Σ9,(114)[1$\bar{1}$0][22$\bar{1}$]	1.60	3.57	3.25	2.03	1.57	3.74	3.40	2.16	1.38	2.74	4.64	-
Σ17b,(2$\bar{2}$3)[110][3$\bar{3}\bar{4}$]	1.60	2.33	2.12	1.33	1.61	2.43	2.21	1.37	-	-	-	-
Σ17b,(3$\bar{3}$4)[110][$\bar{2}$23]	1.59	2.37	2.15	1.36	1.60	2.47	2.24	1.40	-	-	-	-

REFERENCES

1. B.-J. Lee and M. Baskes, "Second nearest-neighbor modified embedded-atom-method potential," Phys. Rev. B **62**, 8564 (2000).
2. B.-J. Lee, M. Baskes, H. Kim, and Y. K. Cho, "Second nearest-neighbor modified embedded atom method potentials for bcc transition metals," Phys. Rev. B **64**, 184102 (2001).
3. M. I. Baskes, J. E. Angelo, and C. L. Bisson, "Atomistic calculations of composite interfaces," **2**, 505–518 (1994).
4. M. Baskes, "Atomistic potentials for the molybdenum–silicon system," Mater. Sci. Eng. A **261**, 165–168 (1999).
5. H.-K. Kim, W.-S. Jung, and B.-J. Lee, "Modified embedded-atom method interatomic potentials for the Fe–Ti–C and Fe–Ti–N ternary systems," Acta Materialia **57**, 3140–3147 (2009).
6. J. H. Rose, J. Ferrante, and J. R. Smith, "Universal binding energy curves for metals and bimetallic interfaces," Phys. Rev. Lett. **47**, 675–678 (1981).
7. S. M. Valone, M. I. Baskes, and R. L. Martin, "Atomistic model of helium bubbles in gallium-stabilized plutonium alloys," Phys. Rev. B **73**, 214209 (2006).
8. C. Barrett and R. Carino, "The MEAM parameter calibration tool: an explicit methodology for hierarchical bridging between ab initio and atomistic scales," Integrating Mater. Manuf. Innov. **5** (2016).
9. C. Kittel, P. McEuen, and P. McEuen, *Introduction to solid state physics*, vol. 8 (Wiley New York, 1996).
10. D. R. Lide, *CRC handbook of chemistry and physics*, vol. 85 (CRC press, 2004).
11. W. S. Ko and B. J. Lee, "Origin of unrealistic blunting during atomistic fracture simulations based on MEAM potentials," Philos. Mag. **94**, 1745–1753 (2014).
12. G. Bonny, D. Terentyev, A. Bakaev, P. Grigorev, and D. Van Neck, "Many-body central force potentials for tungsten," Model. Simul. Mater. Sci. Eng. **22**, 22 (2014).
13. L. Romaner, C. Ambrosch-Draxl, and R. Pippan, "Effect of rhenium on the dislocation core structure in tungsten," Phys. review letters **104**, 195503 (2010).
14. C. R. Weinberger, G. J. Tucker, and S. M. Foiles, "Peierls potential of screw dislocations in bcc transition metals: Predictions from density functional theory," Phys. Rev. B **87**, 054114 (2013).
15. G. Kresse and J. Hafner, "*Ab initio* molecular dynamics for liquid metals," Phys. Rev. B **47**, 558–561 (1993).
16. G. Kresse and J. Hafner, "*Ab initio* molecular-dynamics simulation of the liquid-metal amorphous-semiconductor transition in germanium," Phys. Rev. B **49**, 14251–14269 (1994).
17. G. Kresse and J. Furthmüller, "Efficient iterative schemes for *ab initio* total-energy calculations using a plane-wave basis set," Phys. Rev. B **54**, 11169–11186 (1996).
18. G. Kresse and J. Furthmüller, "Efficiency of ab-initio total energy calculations for metals and semiconductors using a plane-wave basis set," Comput. Mater. Sci. **6**, 15 – 50 (1996).
19. P. E. Blöchl, "Projector augmented-wave method," Phys. Rev. B **50**, 17953–17979 (1994).
20. H. J. Monkhorst and J. D. Pack, "Special points for brillouin-zone integrations," Phys. Rev. B **13**, 5188–5192 (1976).
21. M. Methfessel and A. T. Paxton, "High-precision sampling for brillouin-zone integration in metals," Phys. Rev. B **40**, 3616–3621 (1989).
22. J. P. Perdew, K. Burke, and M. Ernzerhof, "Generalized gradient approximation made simple," Phys. Rev. Lett. **77**, 3865–3868 (1996).
23. J. P. Perdew, K. Burke, and M. Ernzerhof, "Generalized gradient approximation made simple [erratum]," Phys. Rev. Lett. **78**, 1396–1396 (1997).
24. S. Starikov, D. Smirnova, T. Pradhan, Y. Lysogorskiy, H. Chapman, M. Mrovec, and R. Drautz, "Angular-dependent interatomic potential for large-scale atomistic simulation of iron: Development and comprehensive comparison with existing interatomic models," Phys. Rev. Mater. **5**, 063607 (2021).
25. T. Ochs, O. Beck, C. Elsässer, and B. Meyer, "Symmetrical tilt grain boundaries in body-centred cubic transition metals: An ab initio local-density-functional study," Philos. Mag. A **80**, 351–372 (2000).
26. H. Ullmaier, P. Ehrhart, P. Jung, and H. Schultz, *Atomic defects in metals*, vol. 3 (Springer, 1991).
27. K. Heinola and T. Ahlgren, "Diffusion of hydrogen in bcc tungsten studied with first principle calculations," J. Appl. physics **107**, 113531 (2010).
28. J. Park, H. Huang, R. Siegel, and R. Balluffi, "A quantitative study of vacancy defects in quenched tungsten by combined field-ion microscopy and electrical resistometry," Philos. Mag. A **48**, 397–419 (1983).
29. R. C. Ehemann, J. W. Nicklas, H. Park, and J. W. Wilkins, "Ab initio based empirical potential applied to tungsten at high pressure," Phys. Rev. B **95**, 184101 (2017).
30. G. D. Samolyuk, Y. Osetsky, and R. Stoller, "The influence of transition metal solutes on the dislocation core structure and values of the peierls stress and barrier in tungsten," J. Physics: Condens. Matter **25**, 025403 (2012).
31. R. Ayres, G. Shannette, and D. Stein, "Elastic constants of tungsten- rhenium alloys from 77 to 298 k," J. Appl. Phys. **46**, 1526–1530 (1975).
32. L. Ventelon, F. Willaime, C.-C. Fu, M. Heran, and I. Ginoux, "Ab initio investigation of radiation defects in tungsten: Structure of self-interstitials and specificity of di-vacancies compared to other bcc transition metals," J. Nucl. Mater. **425**, 16–21 (2012).

33. D. I. Bolef and J. De Klerk, "Elastic constants of single-crystal Mo and W between 77 and 500 k," J. applied Phys. **33**, 2311–2314 (1962).
34. J. Cordwell and D. Hull, "The brittle fracture of [100] axis tungsten single crystals," Philos. Mag. **19**, 951–966 (1969).
35. L. Vitos, A. Ruban, H. L. Skriver, and J. Kollar, "The surface energy of metals," Surf. science **411**, 186–202 (1998).
36. W. Tyson and W. Miller, "Surface free energies of solid metals: Estimation from liquid surface tension measurements," Surf. Sci. **62**, 267–276 (1977).
37. D. Scheiber, R. Pippan, P. Puschnig, and L. Romaner, "Ab initio calculations of grain boundaries in bcc metals," Model. Simul. Mater. Sci. Eng. **24**, 035013 (2016).
38. J. J. Möller, "*Atomistic Simulations on Grain Boundary Fracture in Tungsten Bicrystals*, Diploma Thesis, Friedrich - Alexander - Universität Erlangen - Nürnberg," (2011).
39. J. J. Möller, "Atomistic Simulations of Crack Front Curvature Effects and Crack-Microstructure Interactions," Ph.D. thesis, Friedrich - Alexander - Universität Erlangen - Nürnberg (2017).